

Silicone polymer composites for thermal protection system: fiber reinforcements and microstructures

J.H. Koo¹, M.J. Miller², J. Weispfenning³ and C. Blackmon⁴

Abstract

A new class of silicone polymer matrix composites was evaluated using a simulated solid rocket motor test apparatus. Conversion of this organic silicone polymer to a ceramic (i.e. silica) structure on exposure to flame impingement or high temperature, accounts for its outstanding thermal stability. A research program was aimed to develop and evaluate this new class of thermal protection materials for military applications. This article presents the effects of the type and form of reinforcements on the thermal performance of a novel class of silicone polymer matrix composites. Reinforcement types such as glass, silica, quartz, NextelTM, and NicalonTM were used. Reinforcement forms such as random continuous-fiber mat, chopped-fiber mat, 2-D fabric, 3-D fabric, chopped roving, and broadgood tapes with different ply angles were tested. Detailed microstructural, mass loss, and peak erosion analyses were conducted on the phenolic-based matrix composite (control) and silicone-based matrix composites to understand their protective mechanisms.

Keywords

silicone polymer matrix composites, phenolic polymer matrix composites, thermal protection materials, ablatives, thermal protection systems

Introduction

Background

Thermal protection materials are required to protect structural components of space vehicles during the re-entry stage, missile launching systems, and solid rocket motors (SRMs). A thorough literature survey was conducted in a series of three papers by Koo et al.^{1–3} for different military and aerospace applications. The literature survey was grouped into: (a) numerical modeling,¹ (b) material thermophysical properties characterization,² and (c) experimental testing.³

Numerical modeling literature¹ was further subdivided into groups based on how the ablation models and the computational fluid dynamic analyses were used for different applications. The different application groups were described as thermal protection system (TPS) for spacecraft, ablative material for missile launching systems, internal insulation for SRMs, and nozzle assembly for SRMs. Material properties characterization literature² of various thermophysical

properties relevant to the performance of thermal protection materials was reviewed. The theoretical and experimental techniques used to determine thermophysical properties such as density, specific heat, decomposition kinetic parameters, melt temperature, and thermochemical expansion of polymeric composites were summarized. Additionally, thermophysical properties of selected virgin and charred ablative materials at elevated temperature were presented. Experimental testing literature³ as well as erosion and heat transfer

¹Department of Mechanical Engineering, The University of Texas at Austin, Texas Materials Institute, Austin, TX 78712-0292, USA

²BAE Systems, Minneapolis, MN 55421-1498, USA

³Cytec Engineered Materials, Winona, MN 55987-2854, USA

⁴Naval Surface Warfare Center, Dahlgren Division, Dahlgren, VA 22448-5100, USA

Corresponding author:

J.H. Koo, Department of Mechanical Engineering, The University of Texas at Austin, Texas Materials Institute, Austin, TX 78712-0292, USA.

Email: jkoo@mail.utexas.edu

Report Documentation Page			Form Approved OMB No. 0704-0188		
Public reporting burden for the collection of information is estimated to average 1 hour per response, including the time for reviewing instructions, searching existing data sources, gathering and maintaining the data needed, and completing and reviewing the collection of information. Send comments regarding this burden estimate or any other aspect of this collection of information, including suggestions for reducing this burden, to Washington Headquarters Services, Directorate for Information Operations and Reports, 1215 Jefferson Davis Highway, Suite 1204, Arlington VA 22202-4302. Respondents should be aware that notwithstanding any other provision of law, no person shall be subject to a penalty for failing to comply with a collection of information if it does not display a currently valid OMB control number.					
1. REPORT DATE 2010	2. REPORT TYPE		3. DATES COVERED 00-00-2010 to 00-00-2010		
4. TITLE AND SUBTITLE Silicone polymer composites for thermal protection system: fiber reinforcements and microstructures			5a. CONTRACT NUMBER		
			5b. GRANT NUMBER		
			5c. PROGRAM ELEMENT NUMBER		
6. AUTHOR(S)			5d. PROJECT NUMBER		
			5e. TASK NUMBER		
			5f. WORK UNIT NUMBER		
7. PERFORMING ORGANIZATION NAME(S) AND ADDRESS(ES) Naval Surface Warfare Center,Dahlgren Division,Dahlgren,VA,22448-5100			8. PERFORMING ORGANIZATION REPORT NUMBER		
9. SPONSORING/MONITORING AGENCY NAME(S) AND ADDRESS(ES)			10. SPONSOR/MONITOR'S ACRONYM(S)		
			11. SPONSOR/MONITOR'S REPORT NUMBER(S)		
12. DISTRIBUTION/AVAILABILITY STATEMENT Approved for public release; distribution unlimited					
13. SUPPLEMENTARY NOTES					
14. ABSTRACT A new class of silicone polymer matrix composites was evaluated using a simulated solid rocket motor test apparatus. Conversion of this organic silicone polymer to a ceramic (i.e. silica) structure on exposure to flame impingement or high temperature, accounts for its outstanding thermal stability. A research program was aimed to develop and evaluate this new class of thermal protection materials for military applications. This article presents the effects of the type and form of reinforcements on the thermal performance of a novel class of silicone polymer matrix composites. Reinforcement types such as glass, silica, quartz, Nextel™, and Nicalon™ were used. Reinforcement forms such as random continuous fiber mat, chopped-fiber mat, 2-D fabric, 3-D fabric, chopped roving, and broadgood tapes with different ply angles were tested. Detailed microstructural, mass loss, and peak erosion analyses were conducted on the phenolic-based matrix composite (control) and silicone-based matrix composites to understand their protective mechanisms.					
15. SUBJECT TERMS					
16. SECURITY CLASSIFICATION OF:			17. LIMITATION OF ABSTRACT Same as Report (SAR)	18. NUMBER OF PAGES 18	19a. NAME OF RESPONSIBLE PERSON
a. REPORT unclassified	b. ABSTRACT unclassified	c. THIS PAGE unclassified			

data relevant to the performance of thermal protection materials for different applications were reviewed. Laboratory scale apparatus, small-scale, and subscale SRMs were used to test these thermal protection materials. In this article, we include only the literature relevant to thermal protection materials used for missile launching systems.

The vertical launching system (VLS) is a special kind of missile launching system used on surface combat ships by the U.S. Navy. It employs individual canisters to store and maintain the missiles in a ready-to-fire condition. The present design of the VLS, originally used for STANDARD missiles and later modified for TOMAHAWK missiles, consists of eight canisters with missiles as well as a plenum chamber and a central uptake duct. Eight missile modules in the VLS, stored beneath the deck of the ship, have separate cell doors over each canister and can be momentarily opened at the time of missile firing. Following the launching of a missile, a two-phase, high temperature and high velocity rocket exhaust plume is produced due to burning of the aluminized propellant in the SRM. The exhaust plume of the SRM travels downward into the plenum chamber and is then directed out of the VLS through the central uptake duct.

The challenge for the integrity, survivability, and maintenance of the VLS is met through its innovative mechanical design and the extensive use of ablative materials. The gas management of the rocket exhaust plume, which is of particular concern in the development of VLS, involves the following issues: strong pressure waves traveling through the canister, and plenum and uptake duct govern the mechanical strength of the design. Turbulent convective heat transfer from the rocket plume provides the largest thermal input on the interior surface of the VLS. In addition, the process of compression and expansion waves decays as a result of the interaction of shock, turbulence, and particle-induced viscous dissipation in the rocket plume.

Yeh⁴ investigated theoretically and experimentally the effect of internal gas flows on material erosion and transient internal ballistic processes in a scaled VLS. As the two-phase plume impinges the ablative material, MXB-360 (phenolic glass mat composite), located at the bottom of the VLS plenum where thermal erosion of the ablative material occurs. Meanwhile, a debris layer, consisting of the liquid-phase aluminum oxides in the plume, forms on the surface of the ablative material, which significantly changes the heat flux to the ablative surface. The theoretical part of this study aims at mathematically formulating the equations governing the behavior of the plume in the VLS plenum, the debris layer between the plume and the ablative material, and the ablative material itself. This coupling model is the first analytical effort to predict the

transient recession on the surface of the ablative material when other erosion models are described by the correlation of the experiment data.

Studies of Yeh⁴ have been focused primarily on the thermochemical ablation. The ablative material used in the VLS environment is not only subjected to a thermal attack but also subjected to a particle impact. Both the mechanical erosion due to the particle impact and the thermochemical ablation caused by the thermal attack can be significant on the surface of the ablative material. To assure the integrity and prolong the lifetime of launcher components, suitable information about the performance of the ablatives that are exposed to this high-temperature, particle-laden flow requires further study.

A transient, 2-D material erosion model was developed by Yang et al.⁵ to describe the simultaneous processes of thermochemical ablation and mechanical erosion of ablative materials. The model predicts the rate of surface recession and the erosion pattern. Numerical calculations of the surface erosion of H41N (phenolic-chopped glass fiber composite) were performed. It was found that particle impact substantially alters the thermochemical ablation and thermal effect also changes the mechanical erosion. The predicted results for overall material erosion of H41N are found to agree reasonably well with available experimental data.

In the preceding studies, the eroded material produced by either thermal ablation or particle impact erosion was assumed to be effectively removed by the ambient gas stream. As such, no melt layer would form on the surface of the material. In reality, however, a melt layer can form on the surface of the material as observed in the experimental studies of Chaboki et al.⁶ and Koo et al.⁷ The composition of the melt layer might include the deposit of the incoming particles and the eroded high-temperature ablative material.

Yang, Cheung, and Koo^{5,8,9} developed a model for the ablative wall material which couples the effects of mechanical erosion due to particle impact and thermochemical ablation. Their model assumes that particles impact and reflect off of the ablative material surface. During the impact, the kinetic energy of the particles is transferred as thermal energy to the surface. They observed that mechanical erosion due to particle impact is comparable in magnitude to thermochemical ablation. Cheung et al.¹⁰ extended the Yang et al. model to include the formation of a layer of molten aluminum oxide on the ablative surface. Cheung et al. calculated the melt layer thickness near a stagnation point by numerically solving integral continuity and momentum equations of the melt layer. The layer acts to protect the ablative surface by slowing down particles before they strike the surface, thus decreasing

mechanical erosion and reducing thermal ablation by increasing the heat transfer resistance.

The use of aluminum to increase the performance of solid propellants yields a two-phase exhaust plume consisting of solid and/or liquid aluminum oxide particles (Al_2O_3) and gaseous combustion products. Some current U.S. Navy rocket motors contain substantial amounts of aluminum to the extent that 40 wt.% of the exhaust products may be composed of Al_2O_3 . These aluminum oxides carry a significant amount of thermal and kinetic energy that is transferred to the launcher when these particles impinge on the launcher walls. Highly localized erosion occurs where aluminized plumes impinge directly on the launcher wall. A thin layer of Al_2O_3 has been observed to form on the launcher walls. Exactly how this layer develops and affects surface heat transfer and ablation is still unresolved. In the early stages of a missile launch, liquid aluminum particles transport a significant amount of thermal energy to the walls. Later, after the melt layer thickens, the layer of Al_2O_3 may actually shield the walls from the exhaust plume. This layer must be modeled accurately to estimate heat transfer from the plume to the launcher walls and predict ablation of the launcher walls.

A typical flow inside a VLS is highly complex and contains mixed supersonic and subsonic regions, various shock structures, turbulent shear layers, and recirculation regions. The Al_2O_3 particles possessing greater momentum and thermal inertia than the gaseous flow, generally lag the gaseous flow in regions of velocity and temperature gradients. There have been attempts at the Naval Surface Warfare Center Dahlgren Division to model the launcher flow using a time-dependent, fully coupled two-phase Navier-Stokes solver, CRAFT.¹¹

York et al.¹² computed particle heat transfer and surface ablation on a flat plate mounted perpendicularly to a plume from an Mk-36 Sidewinder rocket motor. The fully coupled multi-phase Navier-Stokes flow solver CRAFT was used to model the plume impingement. The authors considered both kinetic energy and thermal energy transfer from the Al_2O_3 particles to the ablative material. Total erosion predictions were significantly higher than experimental data. For their calculations, the authors assumed a wall temperature equal to the fail temperature of the ablative material (1600°C). They reasoned that the presence of a layer of molten Al_2O_3 would attenuate the particle heating. Subsequently calculations made assuming a wall temperature of 2300°C (approximately the melt temperature of Al_2O_3) resulted in better agreement with the experimental data.

A model has been developed by Lewis and Anderson¹¹ to predict the formation of a molten Al_2O_3 debris layer in ducted missile launchers.

The model predicts the debris layer thickness and heating to the launcher walls. Integral conservation equations are solved to predict the debris layer thickness and temperature distribution. An implicit finite-difference equation is solved to predict solidification of the debris layer on the launcher walls. The model was validated by predicting erosion of H41N ablative material exposed to the plume of an Mk-36 Sidewinder rocket motor at a standoff distance of 0.91 m. The molten debris layer attenuates heating due to particle impingement and convective heating. The model underpredicted erosion by 25%.

Shih, Cheung, Koo, and Yang¹³⁻¹⁵ developed a physical model to describe the transient ablation phenomenon of high-temperature ablative materials for with and without the formation of a melt layer on the material surface. The model has been applied to H41N (larger heat of ablation) and to MXBE-350 (smaller heat of ablation). When exposed to the same external heat flux, the growth rate of the melt layer for MXBE-350 (phenolic rubber-modified glass composite) is found to be considerably higher than that of H41N. Also, much larger differences in the ablation rates for the cases with and without a melt layer are observed for MXBE-350 when compared to H41N. For a given ablative material the difference in the predicted ablation rates between the cases with and without a melt layer becomes appreciably larger as the imposed external heat flux is increased. When a high-temperature ablative material with a low heat of ablation is exposed to a high external heat flux, the melt layer tends to grow quickly, and as such, a large portion of energy is likely to be trapped within the melt layer under such circumstances. The protective effect of the melt layer cannot be neglected at high external heat fluxes for materials such as MXBE-350 which has small heat of ablation. Additional experimental data are needed to further validate the Shih et al. model.¹⁵

Henderson and co-workers¹⁶⁻²⁷ published a series of papers from 1980 to 1991 which described their thermo-physical properties measurement techniques and numerical modeling as well as thermal data of thermal protection materials for missile launching systems such as H41N and MXBE-350. Henderson and Tant²⁰ reported methods in determining the specific heat, thermochemical expansion, heat of decomposition, and kinetic parameters for both the low-temperature pyrolysis reactions and the high-temperature carbon-silica reactions for MXBE-350.

Henderson and Emmerich²² found experimentally that alteration of the thermophysical properties induced large changes in the thermally induced response of a certain glass-filled polymer composite. The authors reported how to determine the temperature-dependent specific heat of the virgin, char, and

decomposing material and the heat of decomposition of the pyrolysis reactions. Henderson et al.^{22,24,25} used a simultaneous thermal analyzer (STA) to obtain the experimental data and computed the properties using ratio method and numerical integration. Powder ablative samples were machined from larger blocks, then filtered through a sieve, and stored overnight in vacuum at 35°C to remove traces of moisture. To reduce temperature gradient in the material, 10–15 mg of the samples were used and maintained in an argon atmosphere at purge rate of 100 mL/min to prevent thermo-oxidative degradation during testing. All experiments were conducted at heating rates of 20°C/min from 30°C to 1050°C. An empty sample pan was run to establish a baseline for correction. Char samples were obtained by precharring a sample of the virgin material in the STA to 1050°C under the same conditions as the other tests.

Boyer²⁸ developed an implicit finite-difference model to simulate the heat transfer and expansion in charring ablators. Variable thermophysical properties, endothermic decomposition, convective cooling by pyrolysis gases, and thermochemical expansion were accounted in this model. The ablative test sample was instrumented with in-depth thermocouples which recorded temperature. Expansion of the sample was also measured. The radiant heat flux history at the ablator surface was monitored by two radiometers. The data were used to determine the thermophysical properties of MXBE-350 and to validate the accuracy of these properties. The thermophysical properties of MXBE-350 were evaluated by combining the above model and experiment data with a nonlinear estimation algorithm. The specific heat, thermal conductivity, and coefficients of expansion of the ablator and the specific heat of the pyrolysis gas were accurately determined. Both in-depth temperatures and thermochemical expansion were accurately predicted with Boyer's model.

Previous studies by Koo and co-workers^{29–36} have been instrumental in undertaking to study a new class of high-temperature silicone polymer composites and compare them with the more conventional phenolic composites. This article summarizes the portion of the research in which the effects of the type and form of reinforcements as well as the type and amount of fillers on the thermal performance of the silicone polymer matrix composite. Reinforcement types such as glass, silica, quartz, NextelTM, and NicalonTM were used. Reinforcement forms such as random continuous-fiber mat, chopped-fiber mat, 2-D fabric, 3-D fabric, chopped roving, and broadgood tapes with different ply angles were tested using the high-temperature simulated solid rocket motor (SSRM) test apparatus. Silica and alumina fillers of different amounts were evaluated. Detailed microstructural analyses using scanning

electron microscope (SEM) were conducted on the phenolic-based and silicone-based matrix composites to understand their protective mechanisms and their comparative ablation performance using SSRM. Peak erosion and mass loss of post-test composite specimens were used as the major criteria to determine the material performance. Selective materials were tested using the scaled ducted launcher (SDL) test apparatus under solid propellant rocket exhaust plume.³⁷ The overall development and evaluation of this novel class of silicone polymer matrix composites can be found in Koo et al.³⁷

Materials: constituents and fabrication

Polymer system

Silicone polymers can be converted into ceramics through high thermal heating applications.³⁸ This method has been used to prepare ceramic parts and obtain ceramic fibers. Limited work has been reported on the development of fiber-reinforced silicone composites.

A new class of thermal protection materials based on silicone polymers was developed. This family of materials is coded as 'SM8000.' The silicone polymers used are generically categorized as polysiloxanes.^{39,40} Figure 1 shows the chemical structures of this silicone polymer system and consists of a homopolymer and a copolymer of polysiloxanes. The curing of these polymers is facilitated by a catalyst. Curing involves the 'crosslinking' of polymer chains to form a rigid 3-D polymer network. With exposure to high temperatures or flame impingement, the organic polymer decomposes with the evolution of volatile compounds (i.e. water, methanol, and carbon dioxide). Silica (SiO₂) is formed during this process.

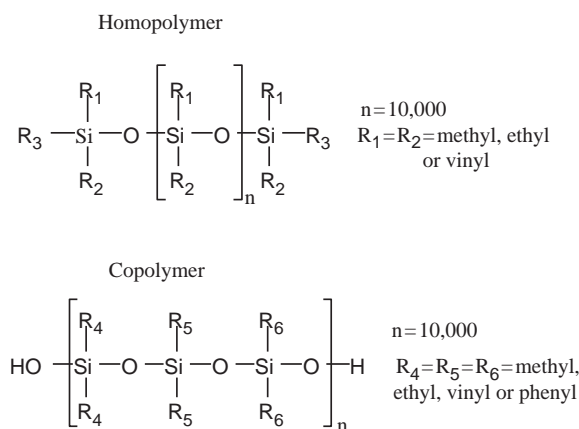


Figure 1. Chemical structures of 'SM8000' silicone polymer.

A resin matrix formulation based on silicone polymers that provided good processability and excellent thermal protection characteristics has been successfully developed. The silicone resin matrix is prepared by blending the silicone polymers, catalyst, and filler (silica or alumina). The blend is then used to impregnate the reinforcing fibers. The impregnated fibers are referred to as 'prepreg.' At this stage, no chemical reaction of the polymers in the resin blend has occurred. Hitco Technology is the original proprietor of the silicone polymer composition. This silicone polymer matrix technology was subsequently licensed to Cytec Engineered Materials, Inc.

Fabrication of silicone polymer matrix composites

The silicone matrix resin is prepared by blending the silicone polymers, catalyst, and filler. The blend is then used to impregnate reinforcing fibers. These fibers can be either glass, silica, quartz, Kevlar®, carbon, or other types of fiber. The fibers can be configured in a variety of forms or 'architectures,' i.e., fabrics, mats, unidirectional arrays, braids, or 3-D structures. The impregnated fiber is known as 'prepreg.' Impregnation of the various fibers is carried out by conventional hot-melt prepregging and solution techniques. Table 1 summarizes the various formulations investigated in the study. The molding compound (MC) versions were made by chopping impregnated fabric into squares with dimensions of $1.27 \times 1.27 \text{ cm}^2$.

Composite laminates are prepared by stacking a number of plies of prepreg in a predetermined sequence. The prepreg stack is then subjected to

curing, either by compression or autoclave molding. Typical cure cycles for the SM8000 laminates are in the following steps: (a) apply vacuum and 1.03 MPa pressure; (b) ramp for room temperature (RT) to 130°C and hold for 1 h to debulk and gel panel; (c) ramp from 135°C to 191°C and hold for 2 h to cross-link the resin; and (d) postcure (freestanding) at 260°C is optional.

Fabrication of $0.91 \times 0.91 \text{ m}^2$ panels was demonstrated for both 0° ply orientation of SM8024 and 30° shingle angle SM8027 and SM8029. All of the initial development work was evaluated on panels of 0.138 m^2 maximum. The selected scale-up material, SM8029 30° shingle angle laminate fabrication was scaled up in three stages to a surface area of 2.98 m^2 as follows: (a) Stage 1: $0.91 \times 0.91 \text{ m}^2$ laminates (0.83 m^2); (c) Stage 2: $1.52 \times 1.22 \text{ m}^2$ laminates (1.85 m^2); and (c) Stage 3: $2.44 \times 1.22 \text{ m}^2$ laminates (2.98 m^2).^{37,41}

Thermal performance testing

Simulated solid rocket motor

An SSRM was used to evaluate the thermal performance of the candidate materials. The SSRM is an established test apparatus developed earlier by Koo et al.⁷ and has been used extensively in our previous studies.^{29–31,34–37,41–44} The SSRM is a small-scale, liquid-fueled rocket motor burning kerosene oxygen as shown in Figure 2. Alumina (Al_2O_3) particles are injected into the plume to simulate the particle-laden flow of solid rocket exhaust. The SSRM is a controlled laboratory device capable of producing a particle-laden exhaust environment with measured heat fluxes from 2840 to $13,728 \text{ kW/m}^2$. The flame temperature is approximately 2200°C and the velocity of the particle-laden exhaust is approximately 2000 m/s.

Table 1. SM8000 variants

Constituent	Example
Matrix resin	Silicone polymers
Filler	Silica, alumina
Fiber type	Glass, silica, quartz, Nextel™, and Nicalon™
Fiber architecture	Mat, fabric, angle interlock, roving, and MC
Laminate ply angle	0° , 30° , 60° , and 90°
SM8000 material code	SM8024 – glass mat, SM8027 – silica fabric, SM8027A – silica roving, SM8027MC – silica chopped fabric, SM8029 – quartz fabric, SM8029A – quartz roving, SM8029MC – quartz chopped fabric, SM8029C – 3-D quartz fabric, SM8032 – Nextel™ 312 fabric, and SM8033 – Nicalon™ fabric

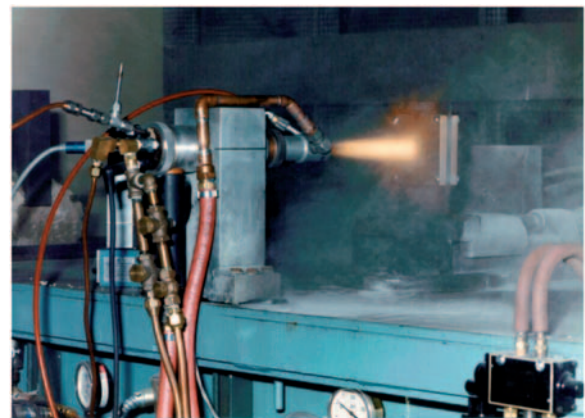


Figure 2. SSRM testing ablative.

The standard sample size is $10.2 \times 10.2 \text{ cm}^2$ and 1.3 cm thick. The composite materials are bonded to $10.2 \times 10.2 \times 0.32 \text{ cm}^3$ steel substrate. A narrow slot is machined into the bondline side of the steel substrate. Two thermocouples are embedded into this slot. The beads of the thermocouples are placed at the center point of the plate. The temperature history of the bondline is recorded with these thermocouples.

The test samples were placed in a fixture downstream from the SSRM nozzle. The fixture has adjustments in axial distance and impingement angle with reference to the plume centerline. A normal (90°), 60° , 20° , and 0° impingements were used for this study. Three axial distances were used to correspond with heat fluxes of 2838, 7094, and $11,345 \text{ kW/m}^2$. Test duration of 12 s was used. Starting prior to the motor burn, the bondline temperature history was recorded for 10 min. Peak erosion was determined by pre- and post-test measurements using a pencil-point dial indicator. Mass loss was determined by pre- and post-test weight loss measurements. Consistent data sets were averaged and are presented in this study.

Microstructural char characterization

In this research program, seven SSRM and three SDL motor firings were conducted.^{37,41} In the first three SSRM firing rounds (Rounds 1–3), they were set to compare the phenolic-based composite (MXBE-350) and different variants of silicone-based composites (SM8000) at the same test conditions. Detailed morphological characterization using SEM was performed to understand the material pre-test (virgin) and post-test (char) microstructures and their protective mechanisms. SEM is a JOEL 5601 and SEM specimens were coated with gold–palladium to reduce electron charging. This article summarizes the detailed microstructural analyses of the first three SSRM firing rounds (Rounds 1–3). A different objective was set for each of these seven SSRM rounds. For the last four SSRM firing rounds (Rounds 4, 5, 7, and 9), 69 SM8000 samples were tested along with 24 MXBE-350 control samples. Peak erosion and mass loss material data of the SSRM firings are included in this article. In addition, three SDL firing rounds (Rounds 6, 8, and 10) consisted of 15 test firings were conducted. Fifty-three SM8000 samples along with 79 MXBE-350 control samples were tested in this research program. A different objective was also set for each of the three SDL rounds. SDL test results will be discussed elsewhere.^{37,41}

Round 1 SSRM firing

In Round 1, MXBE-350 and SM8024 materials were tested using the SSRM at the same conditions to

compare their thermal performance. The SSRM test conditions were 7094 kW/m^2 , 4.5 kg/h alumina particles, and 90° impingement angle for test duration of 12 s. Analyses of post-test MXBE-350 sample at magnifications of $50\times$ and $350\times$ showing glass fibers were exposed after the phenolic resin was eroded when exposed to the extreme temperatures generated by the SSRM. The surface views of the post-test SM8024 sample at $50\times$ and $350\times$ magnifications show some melting of the silicone resin and no glass fibers exposing on the surface as compared to MXBE-350. The cross-sectional views at $350\times$ of the MXBE-350 and SM8024 materials also show more exposure of glass fibers on the surface of the phenolic-based than the silicone-based matrix composites. It was noticed that the thermal wave penetrated deeper into the MXBE-350 than the SM8024 indicating SM8024 was less affected by the extreme heat. From the microstructural analyses of the post-test specimens, it was observed that the protective mechanisms of the phenolic-based and silicone-based ablatives under these extreme heating environments are very different. The silicone resin is more thermally stable than the phenolic resin when exposed to extreme heat. As a result, the SM8024 composite is more ablation resistant than the MXBE-350 composite both on post-test mass loss and average erosion results.^{37,41}

Round 2 SSRM firing

In Round 2, cross-sectional views at $350\times$ of the virgin MXBE-350 (phenolic glass mat) [Figure 3(a)], SM8024 (silicone glass mat) [Figure 3(b)], SM8027 (silicone silica fabric) [Figure 3(c)], SM8027A (silicone silica roving) [Figure 3(d)], SM8027MC (silicone silica MC) [Figure 3(e)], SM8029 (silicone quartz fabric) [Figure 3(f)], and SM8029MC (silicone quartz MC) [Figure 3(g)] were examined using SEM. The different fiber architectures can be clearly seen from this set of SEM micrographs. This set of SM8000 materials were tested using SSRM under the same test conditions. They were exposed to heat fluxes of 6240 and 9643 kW/m^2 with 4.5 kg/h of alumina particles at an impingement angle of 90° for test duration of 12 s.

A series of SEM micrographs at $50\times$, $350\times$, and $1000\times$ of the surface views of MXBE-350 tested at 6240 kW/m^2 show the phenolic resin was pyrolyzed exposing the glass mat on the surface. A similar series of SEM micrographs of MXBE-350 tested at 9643 kW/m^2 [Figure 4(a) and (b)] show more glass mat exposed and some melting of phenolic resin at higher heat flux level. Cross-sectional views of MXBE-350 at $350\times$ exposed to 6240 and 9643 kW/m^2 (Figure 5) were analyzed. No melting of the phenolic resin underneath the surface was observed at 6240 kW/m^2 test case and

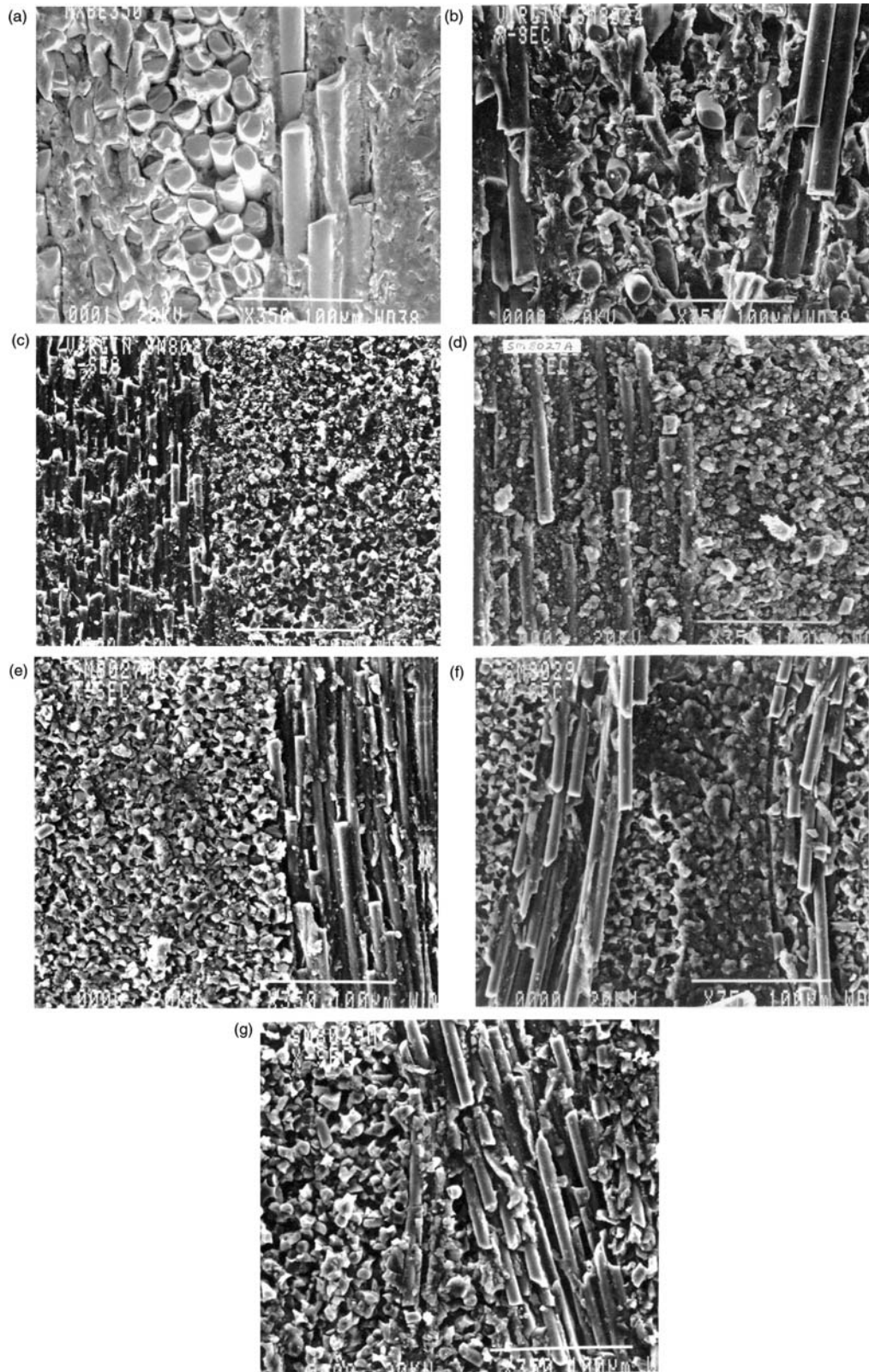


Figure 3. Cross-sectional view of (a) virgin MXBE-350 sample at 350 \times ; (b) virgin SM8024 sample at 350 \times ; (c) virgin SM8027 sample at 350 \times ; (d) virgin SM8027A sample at 350 \times ; (e) virgin SM8027MC sample at 350 \times ; (f) virgin SM8029 sample at 350 \times ; and (g) virgin SM8029MC sample at 350 \times .

Note: Scale bar is 100 μm .

more phenolic melting was observed underneath the surface at the more severe 9643 kW/m^2 test case (Figure 5). Melting of phenolic resin occurred as deep as 0.77 mm from the surface (Figure 5).

A series of SEM micrographs at $50\times$, $350\times$, and $1000\times$ were analyzed showing the surface views of SM8024 (silicone glass mat) tested at 6240 kW/m^2 . Silicone resin melted and a lot of alumina particles were trapped with the melted silicone with no glass fibers exposing on the surface. Another series of SEM

micrographs of SM8024 tested at 9643 kW/m^2 [Figure 6(a) and (b)] show the similar phenomenon as observed at 6240 kW/m^2 test case. Cross-sectional views of SM8024 at $350\times$ exposed to 6240 and 9643 kW/m^2 (Figure 7) were analyzed. More melting of the silicone resin and voids was observed underneath the surface at the 9643 kW/m^2 test case (Figure 7) than the 6240 kW/m^2 test case.

A series of SEM micrographs at different magnifications of the surface views of SM8027 (silicone silica

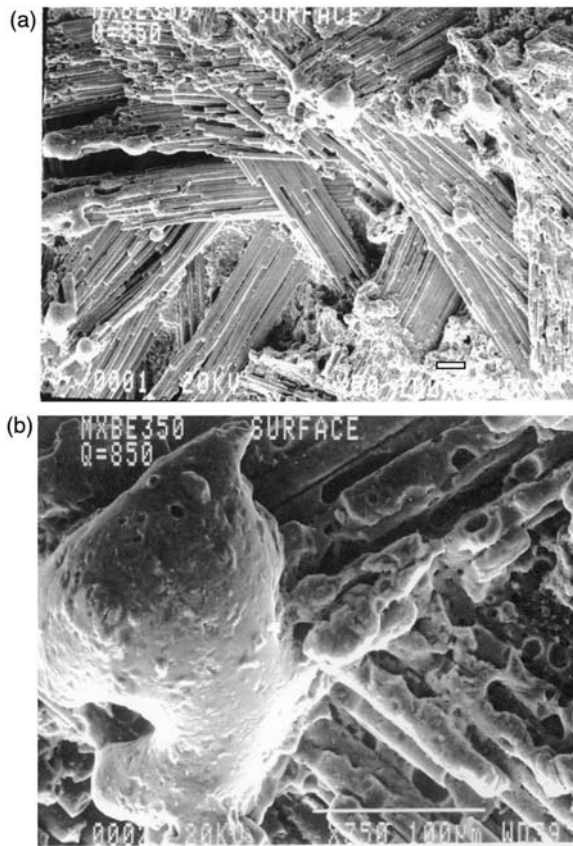


Figure 4. Surface view of MXBE-350 sample at (a) $50\times$ tested at 9643 kW/m^2 ; (b) $350\times$ tested at 9643 kW/m^2 . Note: Scale bar is $100 \mu\text{m}$.

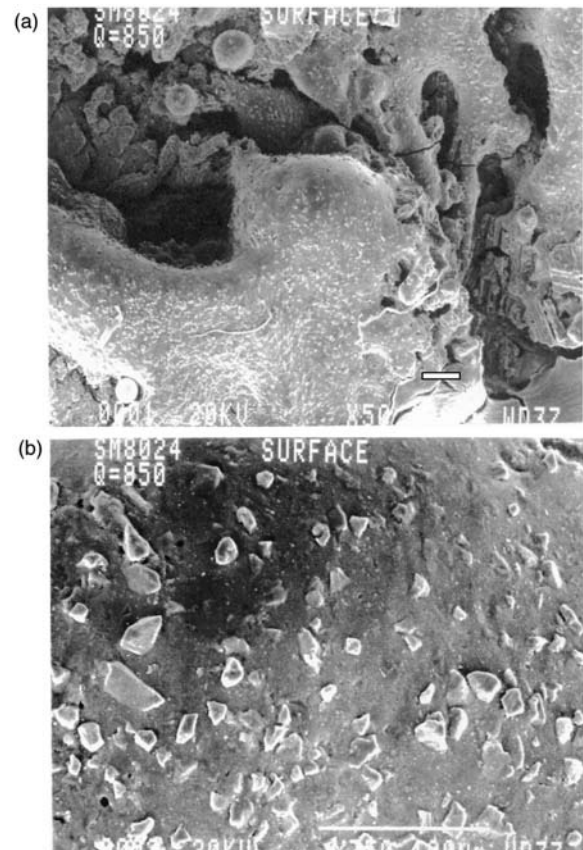


Figure 6. Surface view of SM8024 sample at (a) $50\times$ tested at 9643 kW/m^2 ; (b) $350\times$ tested at 9643 kW/m^2 . Note: Scale bar is $100 \mu\text{m}$.

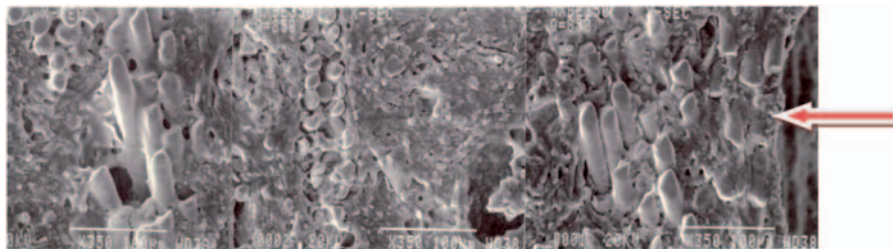


Figure 5. Cross-sectional view of MXBE-350 sample at $350\times$ tested at 9643 kW/m^2 showing thermal wave moving from right to left across the specimen (scale bar is $100 \mu\text{m}$).

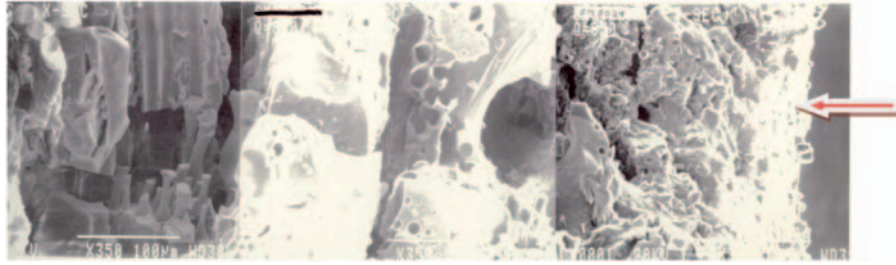


Figure 7. Cross-sectional view of SM8024 sample at 350 \times tested at 9643 kW/m² showing thermal wave moving from right to left across the specimen (scale bar is 100 μ m).

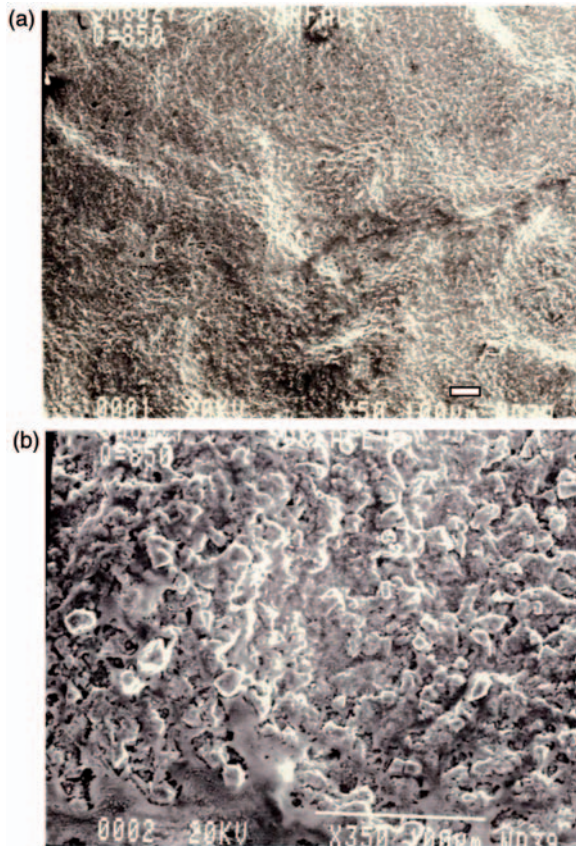


Figure 8. Surface view of SM8027 sample at (a) 50 \times tested at 9643 kW/m² and (b) 350 \times tested at 9643 kW/m².

Note: Scale bar is 100 μ m.

fabric) tested at 6240 kW/m² show the silicone resin was melting and alumina particles were trapped and no silica fibers were exposed on the surface. A series of SEM micrographs of SM8027 at 9643 kW/m² [Figure 8(a) and (b)] show the similar phenomenon as observed at 6240 kW/m². Cross-sectional view of post-test SM8027 sample at 350 \times exposed to 9643 kW/m² is shown in Figure 9. A fair amount of voids appear in between the silica fibers and the silicone resin. It indicated that

the silica fabrics were not totally wetted out in these SM8027 specimens. More melting of the silicone resin and voids were observed at 6240 kW/m² test case than the 9643 kW/m² test case (Figure 9).

A series of SEM micrographs at different magnifications of the surface views of SM8027MC (silicone silica MC) tested at 6240 kW/m² show the silicone resin was melting and alumina particles were trapped on the surface, some silica fibers were exposed, and large cracks are visible on the surface. A similar series of SEM micrographs of SM8027MC at 9643 kW/m² [Figure 10(a) and (b)] show large holes (about 10 μ m) were observed. Cross-sectional view of SM8027MC at 350 \times exposed to 9643 kW/m² is shown in Figure 11. More melting of the silicone resin underneath the surface was observed at 9643 kW/m² test case (Figure 11) than at the 6240 kW/m² test case. Large voids were also observed underneath the surface for the 6240 kW/m² test case.

A series of SEM micrographs at different magnifications of the surface views of SM8029 (silicone quartz fabric) tested at 6240 kW/m² show that the silicone resin was eroded and a small amount of quartz fibers were exposed on the surface. Large holes (about 100 μ m) were observed. A similar series of SEM micrographs of SM8029 at 9643 kW/m² [Figure 12(a) and (b)] show larger holes and cracks were observed. A cross-sectional view of SM8029 at 350 \times exposed to 9643 kW/m² is shown in Figure 13. More melting of the silicone resin and voids was observed underneath the surface at 9643 kW/m² test case (Figure 13) than the 6240 kW/m² test case. The thermal wave penetrates to about 0.8 mm from the front surface of the ablative (Figure 13).

A series of SEM micrographs at different magnifications of the surface views of SM8029MC (silicone quartz MC) tested at 6240 kW/m² show that the silicone resin was eroded. Large holes (10 μ m) and long cracks were observed. A similar series of SEM micrographs of SM8029MC at 9643 kW/m² [Figure 14(a) and (b)] show even larger holes (10–20 μ m) on the surface. A cross-sectional view of SM8029MC at 350 \times exposed

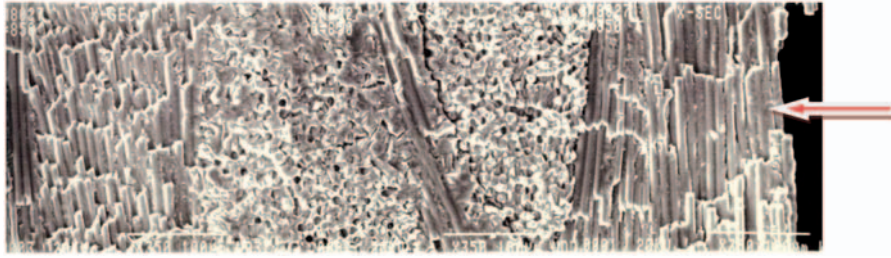


Figure 9. Cross-sectional view of SM8027 sample at 350 \times tested at 9643 kW/m² showing thermal wave moving from right to left across the specimen (scale bar is 100 μ m).

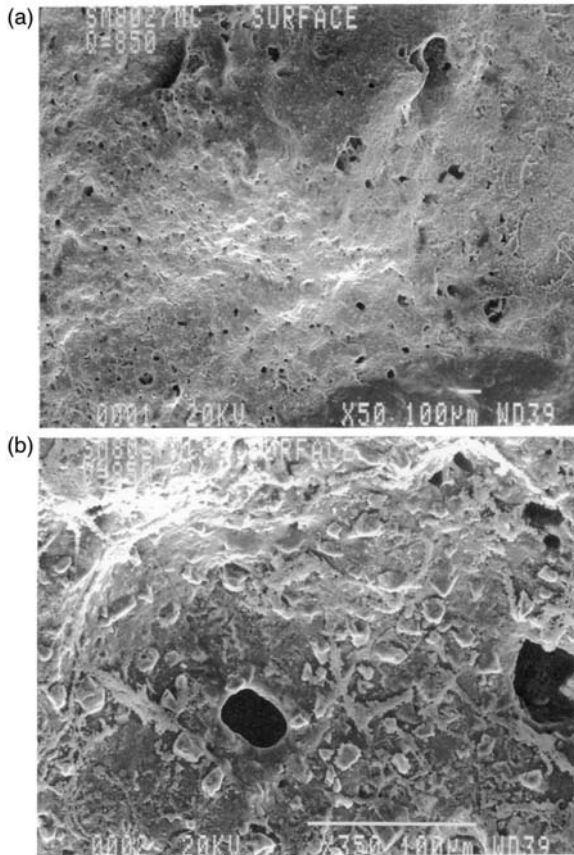


Figure 10. Surface view of SM8027MC sample at (a) 50 \times tested at 9643 kW/m² and (b) 350 \times tested at 9643 kW/m². Note: Scale bar is 100 μ m.

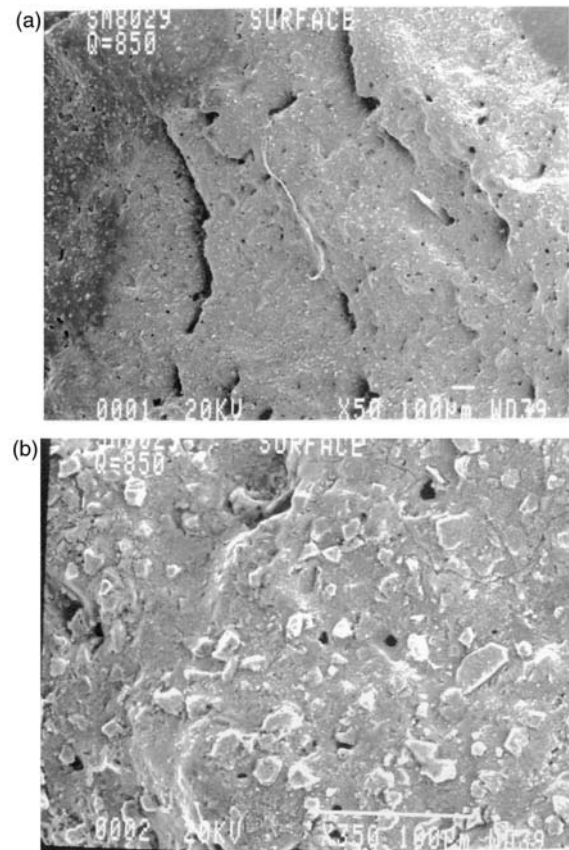


Figure 12. Surface view of SM8029 sample at (a) 50 \times tested at 9643 kW/m² and (b) 350 \times tested at 9643 kW/m². Note: Scale bar is 100 μ m.

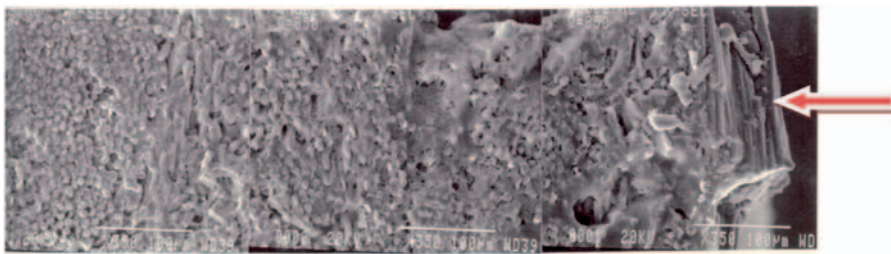


Figure 11. Cross-sectional view of SM8027MC sample at 350 \times tested at 9643 kW/m² showing thermal wave moving from right to left across the specimen (scale bar is 100 μ m).

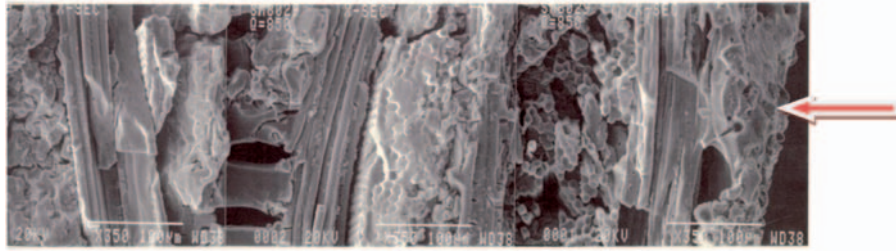


Figure 13. Cross-sectional view of SM8029 sample at 350 \times tested at 9643 kW/m² showing thermal wave moving from right to left across the specimen (scale bar is 100 μ m).

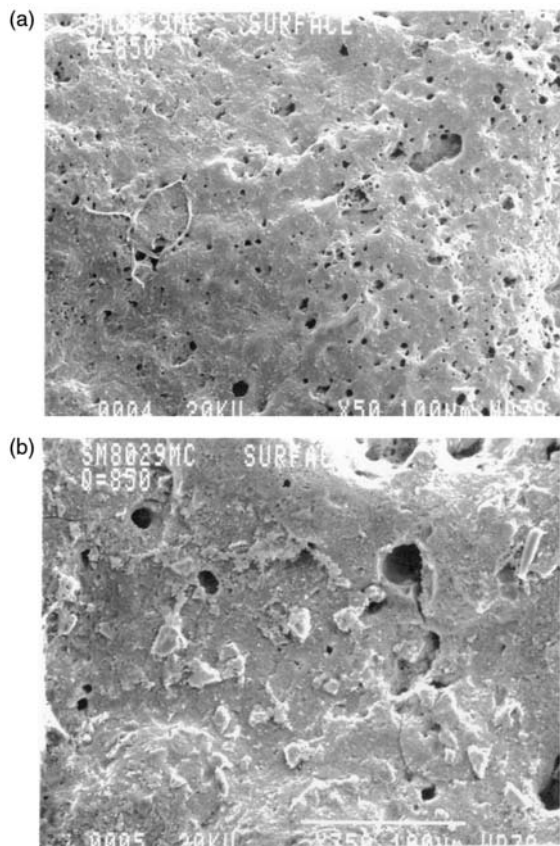


Figure 14. Surface view of SM8029MC sample at (a) 50 \times tested at 9643 kW/m² and (b) 350 \times tested at 9643 kW/m². Note: Scale bar is 100 μ m.

to 9643 kW/m² is shown in Figure 15. Melting of the silicone resin was observed at 9643 kW/m² test case (Figure 15) than at the 6240 kW/m² test case. From Figure 15, this SM8029MC sample shows more quartz fibers and not much silicone resin occurs in between the fibers. It is suspected poor quartz fiber wet out was occurred in this SM8029MC system.

Two sets of ‘ripple firing’ experiments were conducted on MXBE-350 and SM8024 ablative materials. ‘Ripple firing’ is defined as exposing the same ablative material to external heat fluxes for multiple times which

is a real life scenario in the missile launcher. In this study, both MXBE-350 and SM8024 samples were exposed to the same test conditions twice. The test conditions were 6240 kW/m² with 4.5 kg/h alumina for 12 s. Figure 16(a) and (b) shows the MXBE-350 at 50 \times and 350 \times , respectively. Phenolic resin was molten and more glass fibers were observed for this more stringent condition as compared to the ‘single firing’ test case in Figure 4(a) and (b). SM8024 was tested in the same conditions, Figure 17(a) and (b) shows the SM8024 at 50 \times and 350 \times , respectively. A lot of holes and alumina particles were observed on the SM8024 surface, no glass fibers were exposed as seen in the MXBE-350 material. This indicated there was less erosion in the SM8024 than the MXBE-350 specimens. Figures 18 and 19 show the cross-sectional views of the ‘ripple fired’ MXBE-350 and SM8024 specimens, respectively. Large voids underneath the front face were observed in the SM8024 specimen (Figure 19).

Round 3 SSRM firing

In Round 3, MXBE-350 and SM8024 were tested in three levels of heat fluxes 2838, 7094, and 11,350 kW/m² with no alumina particles at 90° impingement for test duration of 12 s. Surface views of MXBE-350 exposing to 2838 kW/m² at 40 \times and 350 \times were analyzed. Melting of phenolic resin and glass fibers were very visible at low heat flux (2838 kW/m²). Surface views of MXBE-350 material exposed to 7094 kW/m² and 11,350 kW/m² at 40 \times [Figure 20(a)] and 350 \times [Figure 20(b)] were analyzed. More large holes and exposed fibers are visible as expected on the MXBE-350 surface as the heat flux increases.

Melting and bubbling as well as cracking of the silicone resin surface are very visible at low heat flux (2838 kW/m²). Surface views of SM8024 material exposed to 7094 and 11,350 kW/m² at 40 \times [Figure 21(a)] and 350 \times [Figure 21(b)] were analyzed. More holes, exposed glass fibers [Figure 21(b)] as well as cracking are visible on the surface as the heat flux increases.

Cross-sectional views of SM8024 and MXBE-350 samples exposed to 2838 kW/m² were analyzed. Large

voids underneath the surface are observed in both the SM8024 and MXBE-350 ablatives. Cross-sectional views of SM8024 and MXBE-350 samples exposed to 7094 and 11,350 kW/m² [Figure 22(a) and (b)] were analyzed. The cross-sectional views of MXBE-350 specimens exposing to the three levels of heat fluxes are very similar in nature with large voids occurring underneath the surface. The SM8024 specimens bear similar observations.

Thermal performance characterization

Mass loss and peak erosion data of SSRM firings

Additional SSRM firings (Rounds 4, 5, and 7) were conducted. A summary of mass loss and peak erosion data of MXBE-350 and SM8000 materials are presented in this section. More detailed discussions can be found in Refs.^{37,41}

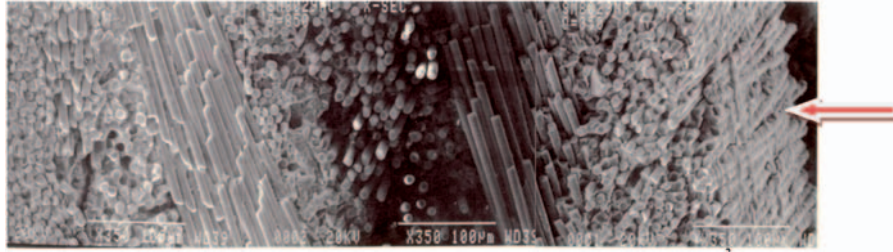


Figure 15. Cross-sectional view of SM8029MC sample at 350 \times tested at 9643 kW/m² showing thermal wave moving from right to left across the specimen (scale bar is 100 μ m).

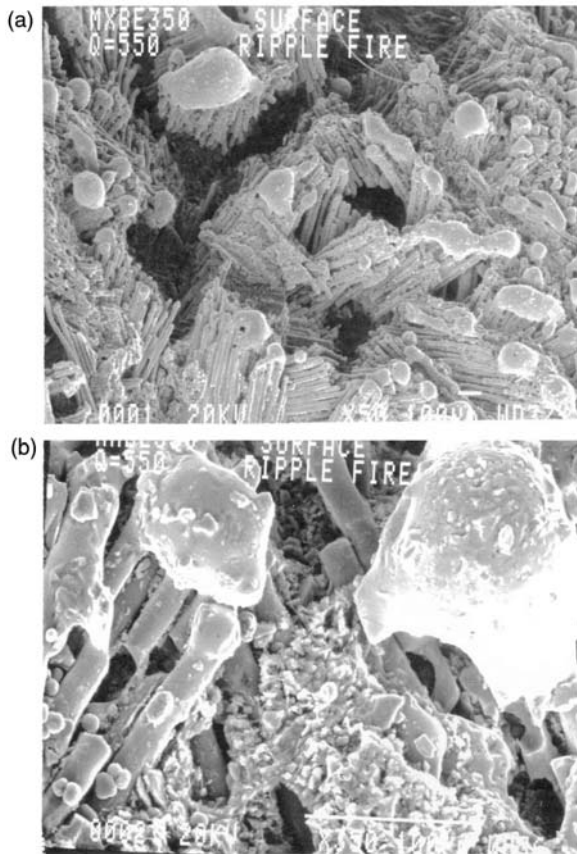


Figure 16. Surface view of MXBE-350 sample at (a) 50 \times tested at 6240 kW/m² under ripple fire and (b) 350 \times tested at 6240 kW/m² under ripple fire. Note: Scale bar is 100 μ m.

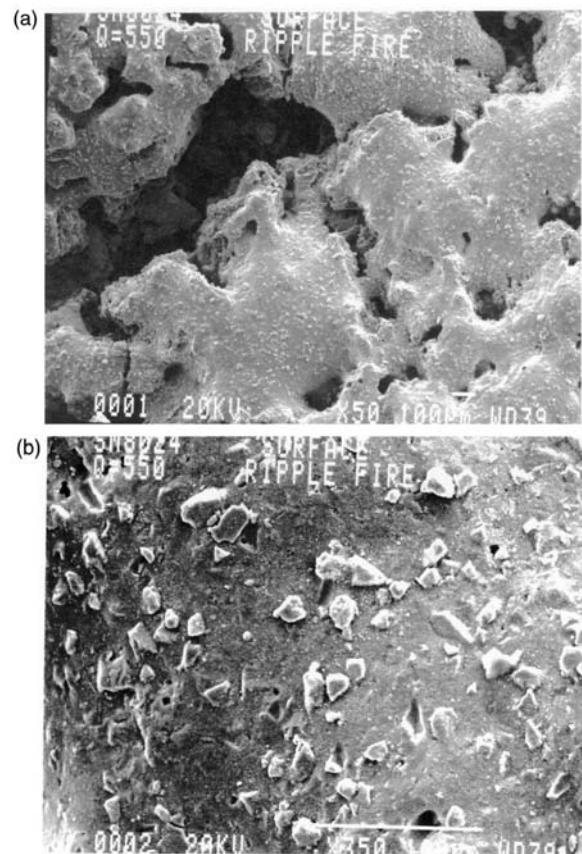


Figure 17. Surface view of SM8024 sample at (a) 50 \times tested at 6240 kW/m² under ripple fire and (b) 350 \times tested at 6240 kW/m² under ripple fire. Note: Scale bar is 100 μ m.

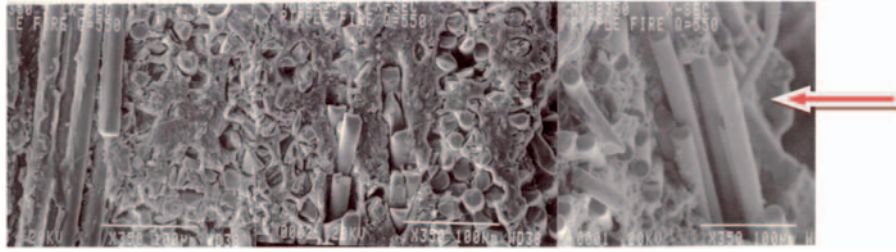


Figure 18. Cross-sectional view of MXBE-350 sample at 350 \times tested at 6240 kW/m² under ripple firing condition with thermal wave is moving from right to left across the specimen (scale bar is 100 μ m).

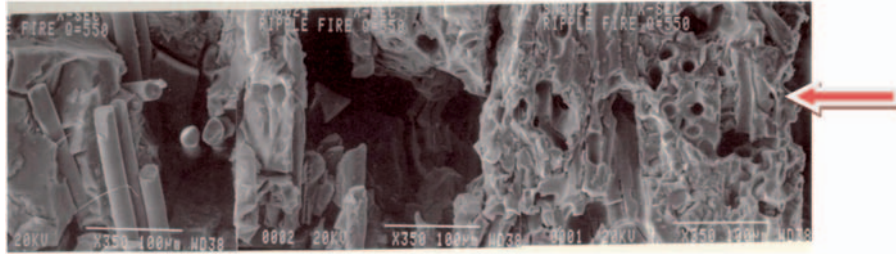


Figure 19. Cross-sectional view of SM8024 sample at 350 \times tested at 6240 kW/m² under ripple firing condition showing thermal wave moving from right to left across the specimen (scale bar is 100 μ m).

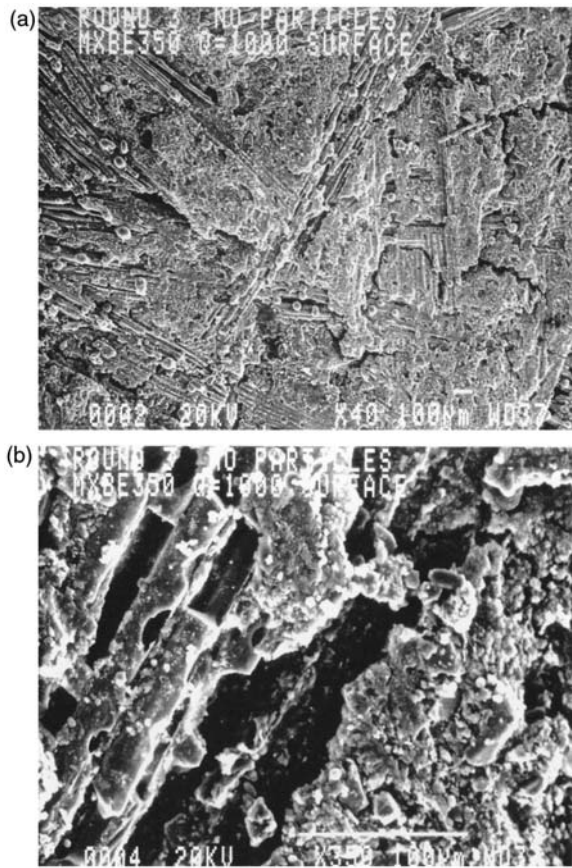


Figure 20. Surface views of MXBE-350 at (a) 40 \times (top) and (b) 350 \times (bottom) tested at 11,350 kW/m² (scale bar is 100 μ m).

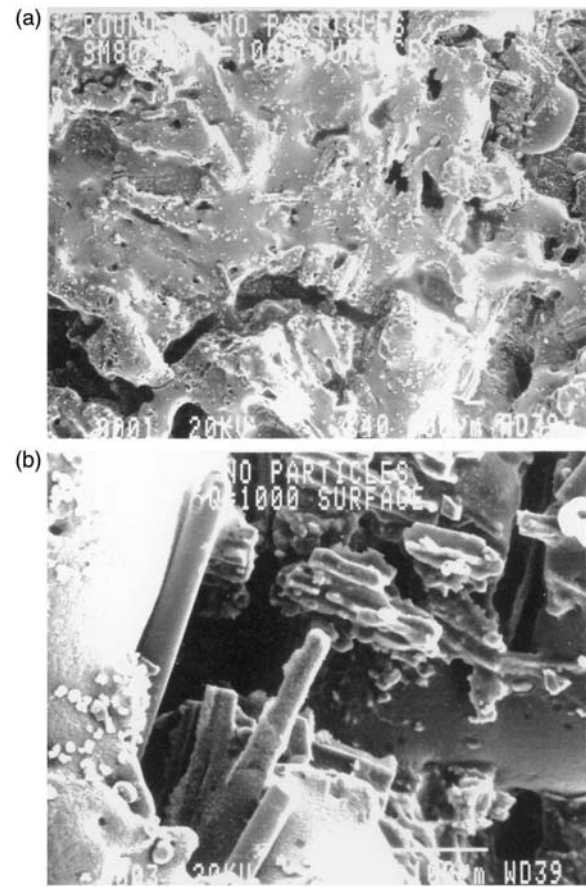


Figure 21. Surface views of SM8024 at (a) 40 \times (top) and (b) 350 \times (bottom) tested at 11,340 kW/m² (scale bar is 100 μ m).

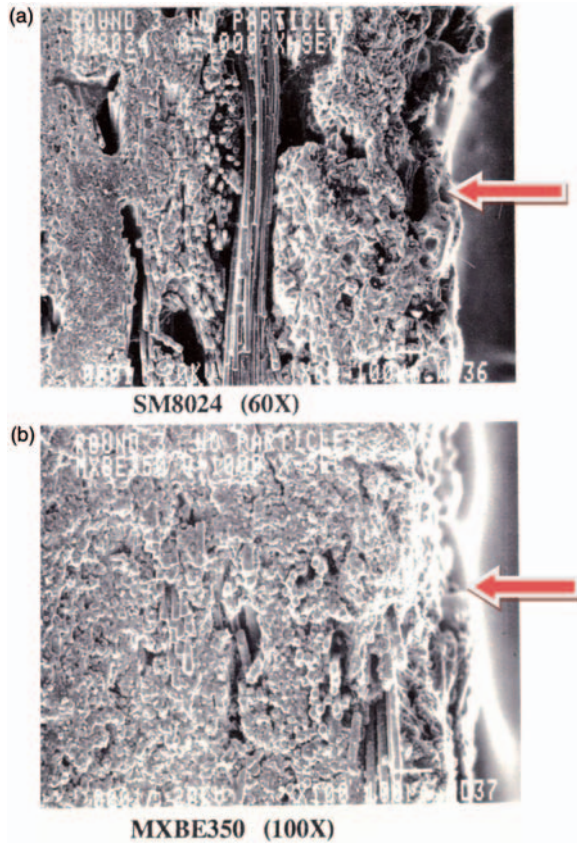
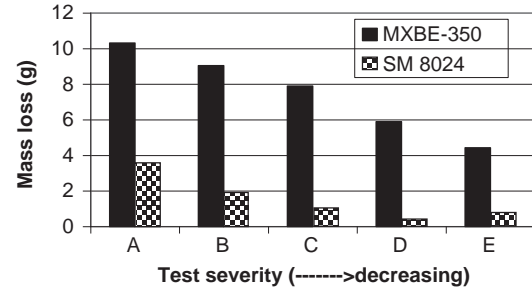


Figure 22. Surface views of (a) SM8024 at 60 \times (top) and (b) MXBE-350 at 100 \times (bottom) tested at 11,350 kW/m² showing thermal wave moving from right to left across the specimen (scale bar is 100 μ m).

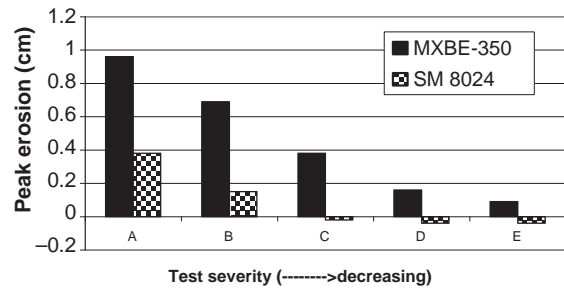
Round 4 was aimed to compare the performance of MXBE-350 and SM8024 under the effects of different heat fluxes and impingement angles. Conditions A is the most severe at 12,480 kW/m², 4.5 kg/h of Al₂O₃, and 90° impingement for test duration of 12 s to the least severe conditions of E at 7094 kW/m², no Al₂O₃, and 20° impingement for test duration of 12 s. Figure 23 shows a comparison in mass loss of SM8024 and MXBE-350 for the five different test conditions. SM8024 clearly shows better performance than MXBE-350. In Condition A, SM8024 has less than 4 g and MXBE-350 has more than 10 g of mass loss. Figure 24 shows a comparison in average peak erosion of SM8024 and MXBE-350 for the five different test conditions. SM8024 has about half of the peak erosion of MXBE-350 in Conditions A and B. In Conditions C, D, and E, SM8024 shows a small amount of swelling.

The following conclusions were drawn: (a) SM8024 gives lower erosion and mass loss (this may also be due to mass of the trapped alumina particles with the molten silicone) under all conditions compared to MXBE-350; (b) flame impingement angle has the



Conditions A = 12,480 kW/m², 4.5 kg/hr Al₂O₃, 90° impingement
Conditions E = 7,094 kW/m², no Al₂O₃, 20° impingement

Figure 23. Round 4 mass loss results of MXBE-350 and SM8024.



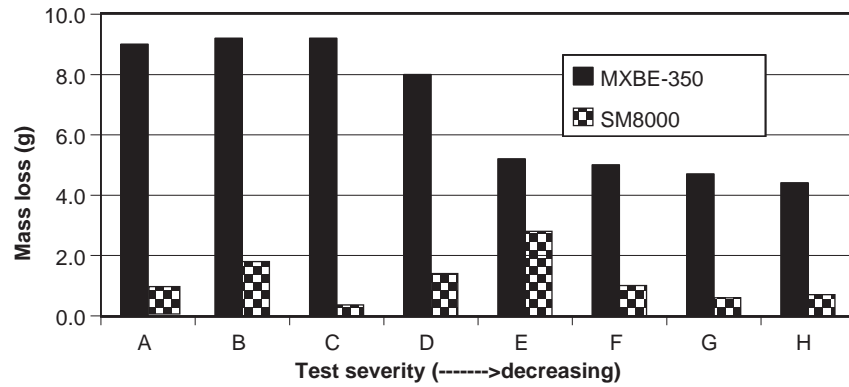
Conditions A = 12,480 kW/m², 4.5 kg/hr Al₂O₃, 90° impingement
Conditions E = 7,094 kW/m², no Al₂O₃, 20° impingement

Figure 24. Round 4 peak erosion results of MXBE-350 and SM8024.

largest effect on all responses and the normal impingement of 90° inflicts the most severe damage; and (c) alumina flow rate has the smallest effect.

Round 5 was undertaken to evaluate the following composite laminate variables: (a) reinforcement type (glass mat, silica fabric, and NextelTM fabric); (b) filler (low, standard, and high levels of silica and alumina where amounts and filler identity are proprietary); and (c) ply angle (90°, 60°, and 20°). SSRM test conditions involved two levels of heat flux 7094 and 12,480 kW/m² and two levels of alumina particle flow rate (0 and 0.9 kg/h) for test duration of 12 s. Figures 25 and 26 show the Round 5 mass loss and peak erosion results. Figure 27 shows the average erosion results of Round 6 where all SM8000 materials outperform MXBE-350.

The following conclusions were drawn: (a) all SM8000 material variants (SM8027, SM8029, and SM8032) outperform MXBE-350 (Figure 27); and (b) within the SM8000 materials and from statistical analysis of the experimental data, these results were observed: (i) fiber orientation of 60° preferred;

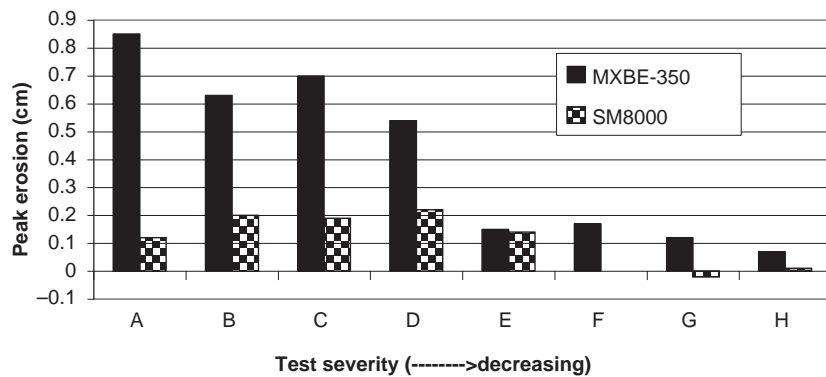


Conditions A=12,480 kW/m², 0.9 kg/hr Al₂O₃, 90° impingement

Conditions H=7,094 kW/m², no Al₂O₃, 20° impingement

SM8000 Variants - highest mass loss of any variant under specified test conditions

Figure 25. Round 5 mass loss results of MXBE-350 and SM8000.



Conditions A=12,480 kW/m², 0.9 kg/hr Al₂O₃, 90° impingement

Conditions H=7,094 kW/m², no Al₂O₃, 20° impingement

SM8000 Variants - highest mass loss of any variant under specified test conditions

Figure 26. Round 5 peak erosion results of MXBE-350 and SM8000.

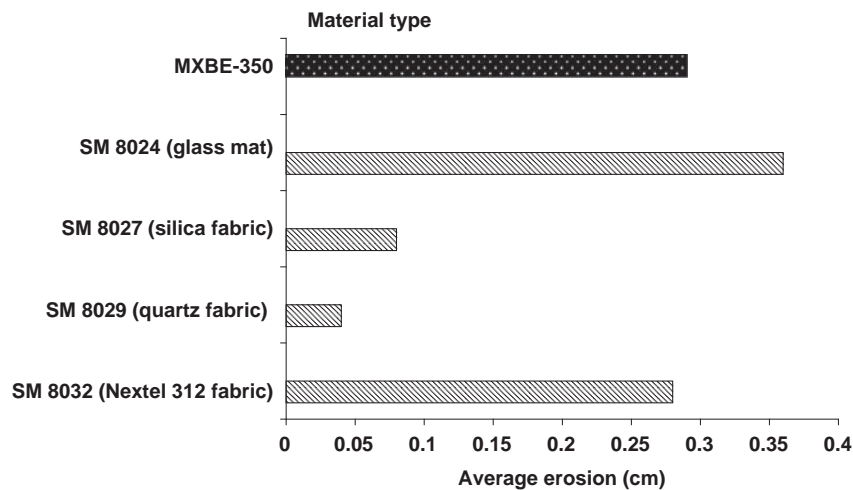


Figure 27. Comparison of Round 6 average erosion results.

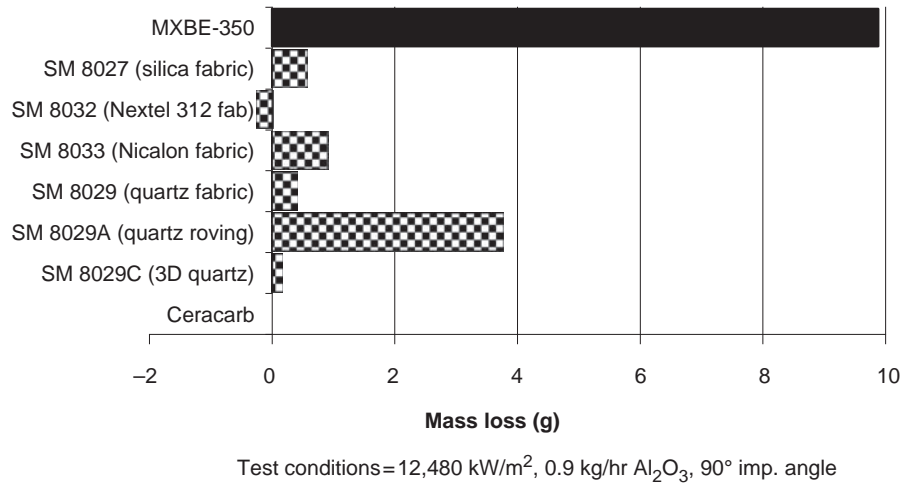


Figure 28. Round 7 mass loss results of candidate materials.

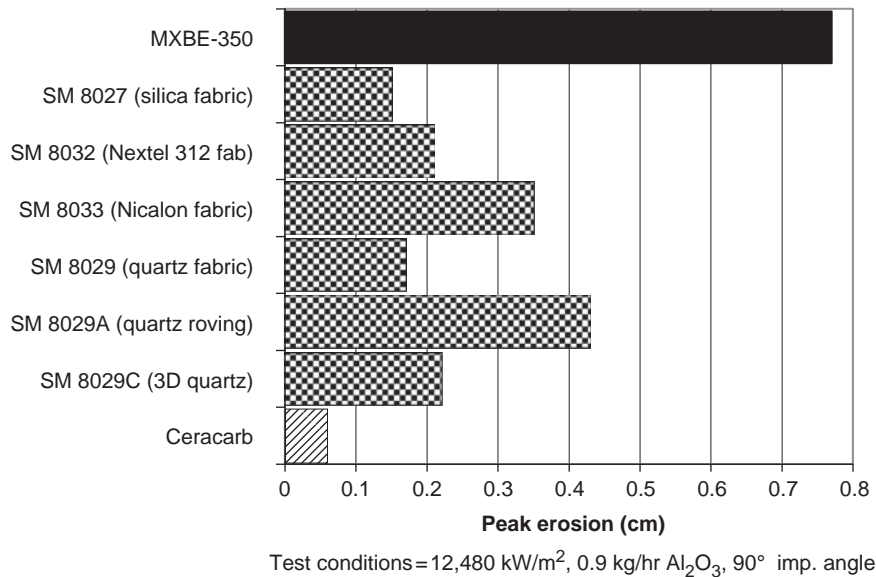


Figure 29. Round 7 peak erosion results of candidate materials.

(ii) impingement angle is important; (iii) low and standard filler (silica) levels preferred; and (iv) best combination for minimizing mass loss and peak erosion (under the most severe test conditions) is NextelTM fabric, 60° ply angle, and low silica filler.

Round 7 was considered to test further 'advanced' material formulations. SM8000 variants, based on high melting, refractory fibers, e.g. NextelTM and NicalonTM were included. Three-dimensional structures were also evaluated. A sample of 'Ceracarb' (SiC-coated C/C with NicalonTM fabric reinforcement) was also tested as an example of a higher performing material. Test conditions were selected as the most severe, i.e. (a) 12,480 kW/m²; (b) 0.9 kg/h Al₂O₃; and (c) 90° impingement angle for a test duration of 12 s.

Figures 28 and 29 show the mass loss and peak erosion results of Round 7.

The following conclusions were drawn: (a) usual high mass loss and erosion noted for MXBE-350; (b) SM8029 (quartz fabric) and SM8027 (silica fabric) performed well; (c) SM8033 (NicalonTM fabric) sample did not perform as well as expected; (d) SM8029A (quartz roving) variant (intended to be equivalent to Cytac Engineered Materials' MXQ-199) did not perform well; (e) SM8029C (3D quartz fabric) performed well; (f) Ceracarb sample (SiC-coated C/C with NicalonTM reinforcement) performed extremely well as expected; and (g) MXB-360 (phenolic glass mat without elastomer modifier) performed well, relative to its MXBE-350 counterpart as expected.

Conclusions

The aims of the SSRM testing of the SM8000 candidate materials for this study were: (a) to evaluate the performance of silicone materials (SM8000) relative to conventional phenolic material (MXBE-350); (b) to determine the effect of formulation variations within the silicone class of materials; (c) to test material reproducibility; and (d) to investigate the effect of flame severity (heat flux and alumina content) to material performance.

In summary, averaging results from SSRM firings yield the following overall conclusions:

- The SSRM device proved capable of delivering reproducible results in a quick and cost-effective manner;
- Microstructural analyses provide insights of the protective mechanisms of the MXBE-350 and the SM8000 materials;
- SM8000 materials always performed substantially better than the MXBE-350 material;
- The silicone resin is more thermally stable than the phenolic resin;
- Both the types of reinforcement and matrix govern the material erosion characteristics, and the silicone system is the preferred polymer matrix;
- The silica fabric (SM8027), quartz fabric (SM8029), and 3D quartz fabric (SM8029C) are the preferred reinforcements for the silicone system.

Acknowledgments

The Office of Naval Research (ONR) sponsored this research under NSWC Contract No. N60921-92-C-A243. Dr C. Blackmon of Naval Surface Warfare Center/Dahlgren Division (NSWCDD) was the program manager. Dr J.H. Koo was employed by BAE Systems (formerly known as United Defense L.P.) while part of this study was performed. Special thanks are due to D. Beckley, Dr D. Wilson, D. Calamito, and J. Siebunshuh who were involved in the research program.

References

1. Koo JH, Ho DWK and Ezekoye OA. A review of numerical and experimental characterization of thermal protection materials – Part I. Numerical modeling. AIAA Paper 2006-4936, 42nd AIAA/ASME/SAE/ASEE Joint Propulsion Conference, Sacramento, CA, July 9–11, 2006.
2. Koo JH, Ho DWK, Bruns MC and Ezekoye OA. A review of numerical and experimental characterization of thermal protection materials – Part II. Property characterization, AIAA Paper 2007-2131, 48th AIAA/ASME/ASCE/AHS Structures, Structural Dynamics, and Materials Conference, Honolulu, HI, April 23–26, 2007.
3. Koo JH, Ho DWK, Bruns MC and Ezekoye OA. A review of numerical and experimental characterization of thermal protection materials – Part III. Experimental testing. AIAA Paper 2007-5773, 43rd AIAA/ASME/SAE/ASEE Joint Propulsion Conference, Cincinnati, OH, July 8–11, 2007.
4. Yeh YP. Studies of the two-phase plume jet and wall erosion in a vertical launching system. PhD Dissertation, Department of Mechanical Engineering, Pennsylvania State University, University Park, PA, 1990.
5. Yang BC, Cheung FB and Koo JH. Numerical investigation of thermo-chemical and mechanical erosion of ablative materials. AIAA Paper 93-2045, 29th AIAA/SAE/ASME/ASEE Joint Propulsion Conference, Monterey, CA, June 28–July 1, 1993.
6. Chaboki A, Kneer MJ, Schneider ME and Koo JH. Supersonic torch facility for ablative testing. AIAA Paper 90-1761, 5th AIAA/ASME Joint Thermophysics and Heat Transfer Conference, Seattle, WA, June 18–20, 1990.
7. Koo JH, Miller MJ, Lin S and Schneider ME. A cost-effective approach to evaluate high-temperature ablatives for military applications. *Naval Eng J* 1992; 104: 166–177.
8. Yang BC. A theoretical study of thermomechanical erosion of high-temperature ablatives. PhD Dissertation, Department of Mechanical Engineering, Pennsylvania State University, University Park, PA, 1992.
9. Yang BC, Cheung FB and Koo JH. Modeling of one-dimensional thermomechanical erosion of the high-temperature ablatives. *Journal of Applied Mechanics* 1993; 60: 1027–1032.
10. Cheung FB, Yang BC, Burch RL and Koo JH. Effect of melt-layer formulation and thermo-mechanical erosion of high-temperature ablative materials. *Proc. Pacific International Conference on Aerospace Science and Technology*, Vol. 1, National Cheng Kung University, Taiwan, December 6–9, 1993, pp.41–48.
11. Lewis D and Anderson L. Effects of melt-layer formation on ablative materials exposed to highly aluminized rocket motor plumes. AIAA Paper 98-0872, 36th AIAA Aerospace Sciences Meeting, Reno, NV, January 1998.
12. York BJ, Sinha N, Dash SM, Anderson LP, Gominho L, Koo JH, et al. Steady/transient plume-launcher interactions and progress towards particulate/surface layer modeling. AIAA Paper 95-0255, 33rd AIAA Aerospace Sciences Meeting, Reno, NV, January 9–12, 1995.
13. Shih YC. Thermochemical ablation of high-temperature thermal insulation materials. PhD Dissertation, Department of Mechanical Engineering, Pennsylvania State University, University Park, PA, 1997.
14. Shih YC and Cheung FB. A numerical study of the thermal response of high-temperature ablative materials. *Numer Heat Transfer, Part A* 1997; 32(5): 555–574.
15. Shih YC, Cheung FB, Koo JH and Yang BC. Numerical study of transient thermal ablation of high-temperature insulation materials. *J Thermophys Heat Transfer* 2003; 17(1): 53–61.
16. Henderson JB. An analytical and experimental study of the pyrolysis of composite ablative materials. PhD Dissertation, Oklahoma State University, Stillwater, OK, 1980.

17. Henderson JB, Tant MR, Moore GR and Wiebelt JA. Determination of kinetic parameters for the thermal decomposition of phenolic ablative materials by a multiple heating rate method. *Thermochim Acta* 1981; 44: 253–264.
18. Henderson JB. An analytical and experimental study of the thermal behavior of polymer composites exposed to high temperature. Final Report submitted to the U.S. Navy Naval Surface Weapons Center, Dahlgren, VA; Dept. of Mechanical Engineering and Applied Mechanics, University of Rhode Island, Kingston, RI, 1984.
19. Henderson JB, Wiebelt JA and Tant MR. A model for the thermal response of polymer composite materials with experimental verification. *J Compos Mater* 1985; 19: 579–595.
20. Henderson JB and Tant MR. Measurement of thermal and kinetic properties of a glass-filled polymer composite to high temperature. *High Temp-High Press* 1986; 18: 17–28.
21. Henderson JB and Wiecek TE. A mathematical model to predict the thermal response of decomposing, expanding polymer composites. *J Compos Mater* 1987; 21: 373–393.
22. Henderson JB and Emmerich WD. Measurement of the specific heat of a glass-filled polymer composite to high temperature. *Thermochim Acta* 1988; 131: 7–14.
23. Henderson JB and Wiecek TE. A numerical study of thermally induced response of decomposing, expanding polymer composites. *Heat Mass Transfer* 1988; 22: 275–284.
24. Florio Jr J, Henderson JB and Test FL. Experimental determination of volumetric heat-transfer coefficients in decomposing polymer composites. American Society of Mechanical Engineers, New York, ASME Paper, 1989.
25. Florio Jr J, Henderson JB and Test FL. Measurement of the thermochemical expansion of porous composite materials. *High Temp-High Press* 1989; 21: 157–165.
26. Florio Jr J, and Henderson JB. Analytical investigation of the thermal response of decomposing polymer composites. *J Thermophys Heat Trans* 1990; 4(4): 485–492.
27. Florio J, Henderson JB, Test FL and Hariharan R. Characterization of forced convection heat transfer in decomposing, glass-filled polymer composites. *J Compos Mater* 1991; 25: 1515–1539.
28. Boyer CT. An analytical and experimental investigation of the thermophysical properties of a swelling, charring composite material. PhD Dissertation, Virginia Polytechnic Institute and State University, Blacksburg, VA, 1984.
29. Wilson D, Beckley DA and Koo JH. Development of new materials for missile launch structures. *JANNAF Propulsion Meeting*, Monterey, CA, November 15–19, 1993.
30. Miller MJ, Koo JH, Wilson D and Beckley DA. Effect of reinforcements in a silicone resin composite. AIAA Paper 94-0787, *32nd AIAA Aerospace Sciences Meeting*, Reno, NV, January 10–13, 1994.
31. Koo JH, Miller MJ, Wilson D and Beckley DA. Performance envelope of a silicone polymer composite. *1994 International SAMPE Symposium and Exhibition*, Vol. 39, Long Beach, CA, May 1994, pp.1576–1589.
32. Miller MJ, Koo JH, Siebenshuh JR, Wilson D and Beckley DA. Development of a scaled ducted launcher for ablative testing. AIAA Paper 95-0256, *31st AIAA/ASME/SAE/ASEE Joint Propulsion Conference*, San Diego, CA, July 10–12, 1995.
33. VanMeter ML, Koo JH, Wilson D and Beckley DA. Mechanical properties and material behavior of a glass silicone polymer composite. *1995 International SAMPE Symposium and Exhibition*, Vol. 40, Long Beach, CA, May 1995, pp.1425–1434.
34. Koo JH, Venumbaka S, Miller MJ, Wilson D, Beckley DA and Calamito D. Effects of major constituents on the performance of silicone polymer composite. *30th International SAMPE Technical Conference*, San Antonio, TX, October 21–24, 1998.
35. Koo JH, Venumbaka S, Miller MJ, Wilson J, Beckley DA, Calamito D, et al. Thermal performance of a class of silicone polymer composites. *1999 International SAMPE Symposium and Exhibition*, Vol. 44, Long Beach, CA, May 23–27, 1999, pp.1431–1441.
36. Koo JH, Venumbaka S, Weispfenning J and Blackmon C. Silicone matrix composites for thermal protection. *31st International SAMPE Technical Conference*, Chicago, IL, October 27–31, 1999.
37. Koo JH, Miller MJ, Weispfenning J and Blackmon C. Silicone polymer composites for thermal protection system: fiber reinforcements, microstructures, and performance. AIAA Paper 2009-5274, *45th AIAA/ASME/SAE/ASEE Joint Propulsion Conference*, Denver, CO, August 2–5, 2009.
38. Baney R and Chandra G. Preceramic polymers. In: *Concise encyclopedia of polymer science and engineering*. New York: Wiley, 1990.
39. Beckley DA and Sites J. U.S. Patent: Processable Silicone Composite Materials Having High Temperature Resistance, Patent No.: 5,552,466, September 3, 1996.
40. Beckley DA and Sites J. U.S. Patent: Processable Silicone Composite Material Having High Temperature Resistance, Patent No.: 5,612,399, March 18, 1997.
41. Koo JH, Miller MJ, Weispfenning J and Blackmon C. Development and evaluation of silicone polymer composites for thermal protection system. *J Spacecr Rockets* 2010; under review.
42. Koo JH, Stretz A, Bray A, Weispfenning J, Luo ZP and Wootan W. Nanocomposites rocket ablative materials: processing, characterization, and performance. *2003 International SAMPE Symposium and Exhibition*, Vol. 48, Long Beach, CA, May 11–15, 2003, pp.1156–1170.
43. Koo JH, Pilato LA and Wissler GE. Polymer nanostructured materials for propulsion systems. *J Spacecr Rockets* 2007; 44(6): 1250–1262.
44. Koo JH and Pilato LA. Thermal properties and microstructures of polymer nanostructured materials. In: Schulz MJ, Kelkar AD and Sundaresan MJ (eds) *Nanoengineering of structural, functional, and smart materials*. Boca Raton, FL: CRC Press, 2006, pp.409–441.